The Astrophysical Journal, 796:28 (14pp), 2014 November 20 doi:10.1088/0004-637X/796/1/28

OBSERVATION AND MODELING OF GEOCORONAL CHARGE EXCHANGE X-RAY EMISSION DURING SOLAR WIND GUSTS

B. J. Wargelin[1], M. Kornbleuth[1,3], P. L. Martin[2], and M. Juda[1]
[1] Harvard-Smithsonian Center for Astrophysics, 60 Garden Street, Cambridge, MA 02138, USA
[2] School of Physics and Astronomy, University of Southampton, Highfield, Southampton, SO17 1BJ, UK
Received 2014 July 25; accepted 2014 September 23; published 2014 October 31

ABSTRACT

Solar wind charge exchange (SWCX) X-rays are emitted when highly charged solar wind ions such as O^{7+} collide with neutral gas, including the Earth's tenuous outer atmosphere (exosphere or geocorona) and hydrogen and helium from the local interstellar medium drifting through the heliosphere. This geocoronal and heliospheric emission comprises a significant and varying fraction of the soft X-ray background (SXRB) and is seen in every X-ray observation, with the intensity dependent on solar wind conditions and observation geometry. Under the right conditions, geocoronal emission can increase the apparent SXRB by roughly an order of magnitude for an hour or more. In this work, we study a dozen occasions when the near-Earth solar wind flux was exceptionally high. These gusts of wind lead to abrupt changes in SWCX X-ray emission around Earth, which may or may not be seen by X-ray observatories depending on their line of sight. Using detailed three-dimensional magnetohydrodynamical simulations of the solar wind's interaction with the Earth's magnetosphere, and element abundances and ionization states measured by *ACE*, we model the time-dependent brightness of major geocoronal SWCX emission lines during those gusts and compare with changes in the X-ray background measured by the *Chandra* X-ray Observatory. We find reasonably good agreement between model and observation, with measured geocoronal line brightnesses averaged over 1 hr of up to 136 photons s^{-1} cm^{-2} sr^{-1} in the O VII Kα triplet around 564 eV.

Key words: solar wind – X-rays: diffuse background

Online-only material: color figures

1. INTRODUCTION

By the 1980s, three contributors to the soft X-ray background (SXRB; $E \lesssim 2$ keV) were recognized: extragalactic emission (an absorbed power law), absorbed $\sim 2 \times 10^6$ K thermal emission from the Galactic halo, and unabsorbed $\sim 10^6$ K emission from hot gas within the Local Bubble (e.g., McCammon et al. 1983; Marshall & Clark 1984; Bloch et al. 1986). In the 1990s, the *ROSAT* X-ray observatory conducted a comprehensive all-sky survey below 2 keV using proportional counters and often detected puzzling long-term enhancements (LTEs) in the SXRB that persisted for a few hours to days (Snowden et al. 1995). By studying the temporal correlation of solar wind flux and LTE intensity, Cravens et al. (2001) showed that LTEs were caused by the same process responsible for cometary X-ray emission (Cravens 1997), namely, charge exchange of highly charged solar wind ions such as fully ionized and hydrogenic C and O with neutral gas.

Subsequent studies, including Lallement (2004), Koutroumpa et al. (2009), Smith et al. (2014), and Galeazzi et al. (2014), examined the contribution of solar wind charge exchange (SWCX) to the SXRB in *ROSAT* 's 1/4 keV band. Such studies rely heavily on modeling with significant uncertainties. The predicted SWCX intensities depend on observation geometry and solar activity, and the SXRB itself varies by factors of several over the sky. However, results generally point to roughly half of the 1/4 keV SXRB arising from SWCX near the Galactic plane with a lower fraction at higher latitudes where distant emission is less absorbed. X-ray missions that followed *ROSAT* (*Chandra*, *XMM-Newton*, *Suzaku*, and *Swift*) have used CCDs, which do not have a useful response in the 1/4 keV band. SWCX/SXRB analyses (e.g., Smith et al. 2007; Henley & Shelton 2008, 2012; Yoshino et al. 2009) using data from those missions have, therefore, focused on oxygen emission near 600 eV. Even when LTE analogs are removed from analysis, a wide range of SXRB O VII Kα intensities are found, typically $\sim$2–10 photons cm^{-2} s^{-1} sr^{-1} (Line Units; LU), with a median value of $\sim$5 LU (Henley & Shelton 2010). Inferred SWCX contributions are usually estimated to be between 1 and 3 LU, most of which comes from heliospheric SWCX and modeled geocoronal intensities of no more than a few tenths of an LU (Henley & Shelton 2008; Slavin et al. 2013).

As explained by Cravens et al. (2001), the most abrupt LTEs are caused by geocoronal SWCX as solar wind ions collide with neutral hydrogen in the Earth's exosphere, or geocorona, within a few tens of Earth radii (R_E). The typical solar wind speed in the ecliptic is $\sim$400 km s^{-1} (Smith et al. 2003); thus, it takes only 2.7 minutes for the wind to traverse $10R_E$, which is consistent with observed SXRB variations on timescales of $\sim$10 minutes (Fujimoto et al. 2007). Cravens et al. (2001) further explain that longer lasting and less abrupt changes in SXRB emission are generally caused by heliospheric SWCX, in which the solar wind collides with neutral H and He in the heliosphere. Most of the observed emission originates over a distance of several AU; since it takes $\sim$4 days for the solar wind to radially traverse 1 AU, spatial averaging means that heliospheric emission typically varies on timescales of days, although faster responses to wind transients may be seen with certain observation geometries (see Section 5).

With the moderate resolution of CCD detectors, SWCX spectra are similar to the thermal spectrum of the Local Bubble with $kT \sim 0.1$ keV (Yoshino et al. 2009). This is not surprising since the source of the solar wind is the solar corona, but SWCX

[3] Current address: Astronomy Department, Boston University, 725 Commonwealth Avenue, Boston, MA 02215, USA.

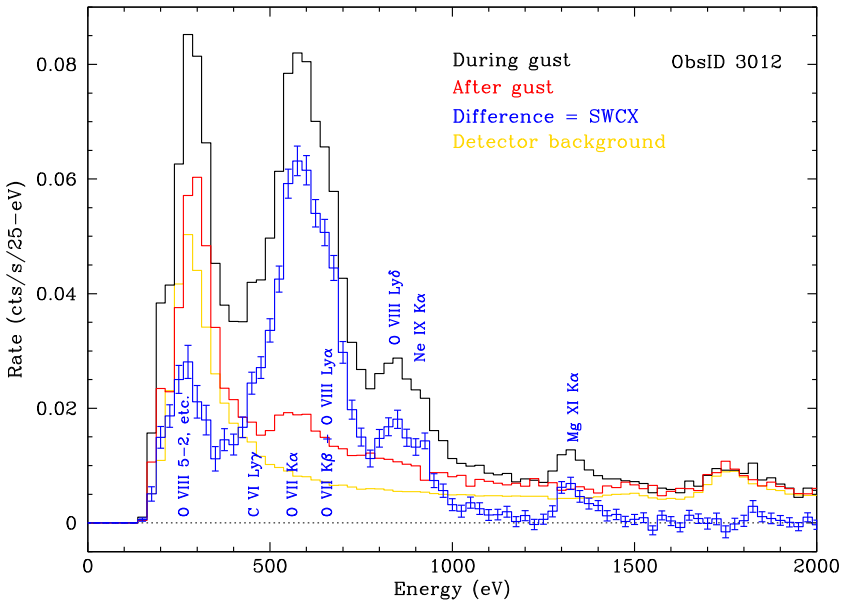

Figure 1. Spectra of ObsID 3012 during and after a strong solar wind gust. The difference is solely due to changes in SWCX emission.
(A color version of this figure is available in the online journal.)

spectra have some distinct features. As highly charged solar wind ions such as O^{7+} collide with neutral gas, they capture an electron into a high-n level, which then decays to ground, either directly or via cascades. This results in enhanced emission of high-n hydrogenic lines such as O VIII Lyδ, and of the forbidden line in He-like triplets such as O VII Kα. More information on charge exchange X-ray spectra may be found in the review article by Wargelin et al. (2008).

Although SWCX emission is present in every X-ray observation, it is usually difficult to isolate it from the nonvarying cosmic background. SWCX spectra can, however, be extracted by comparing low- and high-rate background spectra of the same field, thus removing the constant SXRB components (along with quiescent SWCX emission present in both observations). Examples include Snowden et al. (2004) and Fujimoto et al. (2007), both of which exhibit unusually high-energy emission from Mg XI Kα at 1.34 keV. Figure 1 shows spectra from one of the observations in the present paper, during and after a particularly strong gust of solar wind. Major SWCX lines are labeled, including Mg XI Kα.

Our aim in this work is to quantify changes in X-ray background emission observed by the *Chandra* X-ray Observatory during solar wind gusts, particularly the strong oxygen lines near 600 eV (O VII Kα, O VII Kβ, and O VIII Lyα) which dominate SWCX spectra. We then compare those measurements with model predictions of SWCX emission based on state of the art solar wind/magnetospheric simulations and measured solar wind elements and ion abundances. We explain how we chose the gusts studied here in Section 2, how the corresponding *Chandra* data were analyzed in Section 3, and how geocoronal SWCX emission was modeled in Section 4. In Section 5, we compare the observational and modeling results, followed by conclusions in Section 6.

2. GUST SELECTION

The *Advanced Composition Explorer* (*ACE*) was launched in mid-1997 and began collecting solar wind data near the Sun–Earth L1 point (~0.01 AU toward the Sun) early in 1998. There, it sampled solar wind that, with a typical speed of 400 km s^{-1}, passes by the Earth about one hour later. *ACE* carries several instruments, including the Solar Wind Electron Proton Alpha Monitor (SWEPAM; McComas et al. 1998) and the Solar Wind Ion Composition/Mass Spectrometers (SWICS/SWIMS; Gloeckler et al. 1998). SWEPAM records proton density, velocity, and temperature, as well as the relative abundance of He ions, which make up 2%–5% of the solar wind. Data (version 3.20) are available at http://www.srl.caltech.edu/ACE/ASC/level2/ with 64 s, 1 hr, daily, and 27 day binning. SWICS/SWIMS (data version 3.3.1) records He^{2+} density and velocity, and the relative abundance and charge distribution of trace elements such as C, O, Ne, Mg, Si, and Fe with one hour, two hour, and daily binning.

The most relevant factor in geocoronal SWCX intensity is the flux of X-ray emitting ions, particularly O^{7+}, through near-Earth space. O^{7+} flux can be computed from SWICS data as

$$F_{O^{7+}} = n_{He} v_{He} \frac{n_O}{n_{He}} \frac{n_{O^{7+}}}{n_O}, \quad (1)$$

where n_{He} and v_{He} are the helium ion density and velocity, n_O/n_{He} is the relative abundance of O and He, and $n_{O^{7+}}/n_O$ is the fraction of H-like oxygen ions. The other major variable in computing SWCX intensity is the column density of neutral gas that the solar wind encounters. When the solar wind flux is high, the Earth's magnetosphere is compressed, and ions can reach denser portions of the neutral exosphere where SWCX emissivity is higher. We therefore are also interested in periods of high proton flux, which is computed from SWEPAM data as $n_p v_p$.

Chandra was launched in mid-1999, orbiting between approximately 3 and 20 R_E and spending much of its time outside the magnetosphere. Standard observations began late that year and we searched the *ACE* data archive from 2000 to 2010 for periods of high proton and O^{7+} flux. Solar wind gusts are most common and intense during solar maximum, which occurred in 2000, and very few strong gusts were seen after 2006. We did not look for gusts later than 2010 because of steadily decreasing detector efficiency, caused by contaminant build-up

Table 1
Chandra Observations and Incident Solar Wind Fluxes

ObsID	Starting Date	Raw Exp. (ks)	Clean Exp. (ks)	CCDs[a]	Mode	Max. p Flux[b] (cm^{-2} s^{-1})	Max. O^{7+} Flux[b] (cm^{-2} s^{-1})	l (deg)	b (deg)
430	2000/10/13	39.1	19.9	I23 S123	VF	14.5×10^8	67.9×10^4	70 40 01.7	−32 34 21.2
2232	2001/02/19	129.2	129.0	I0123 S2	F	4.3×10^{8cd}	54.4×10^4	148 21 42.8	+57 17 06.7
2255	2001/09/11	59.4	58.7	I0123 S3	F	15.8×10^{8d}	60.6×10^4	345 10 33.5	−36 54 13.7
2735	2002/09/29	65.2	64.5	I23 S23	F	13.4×10^{8c}	92.4×10^4	311 15 12.0	−62 21 09.7
3012	2002/12/19	42.9	40.9	I23 S123	F	24.1×10^8	90.7×10^4	68 58 08.6	−60 00 04.1
3754	2003/07/25	128.0	94.0	I0123 S23	VF	21.6×10^{8c}	42.9×10^4	270 51 16.1	−00 55 53.6
4215	2003/12/04	66.3	65.3	I0123 S2	VF	7.3×10^{8cd}	84.9×10^4	72 29 55.3	−19 33 03.1
5801	2005/10/24	44.4	43.7	I3 S123	VF	17.6×10^{8c}	60.6×10^4	63 25 18.2	−18 48 48.5
544	2000/03/22	10.3	10.3	I0123 S2	F	25.0×10^8	2.2×10^4	219 46 21.4	+51 55 02.7
4715	2004/12/05	5.7	5.3	I23 S123	VF	33.2×10^8	9.4×10^4	358 22 49.5	−36 30 55.6
6312	2005/06/23	39.6	38.9	I23 S123	VF	30.3×10^8	9.2×10^4	285 23 29.6	+23 54 52.1
6433	2006/09/23	70.4	51.4	I0123 S23	VF	28.4×10^8	9.7×10^4	159 05 54.4	−56 56 51.2

Notes.
[a] The S4 chip, if present, was excluded from analysis—see the text.
[b] Averaging over one hour bins for protons and two hours for O^{7+}.
[c] *Wind* data fill gaps in *ACE* SWEPAM proton data.
[d] Proton density derived in part or whole from *ACE* SWICS He density and interpolated SWEPAM He/H ratio.

on the ACIS filters, at low energies characteristic of SWCX emission.

After identifying ∼100 of the strongest gusts, we then checked which occurred during *Chandra* observations. In order to obtain an adequate X-ray signal for our SWCX analysis, we require observations using the ACIS CCD array with at least three chips, without a transmission grating, for at least 5 ks. With these constraints, and given *Chandra*'s ∼70% observing efficiency, only about one in four gusts is suitable for our study, and this is further reduced to about one in five because some observations have either a problematic detector particle background (see Section 3.1.1) or did not provide enough source-free area. Note that if *Chandra* was orbiting outside the magnetosphere during particularly intense gusts, such as coronal mass ejections, it was likely to be shut down to protect the detectors from damage due to excessive particle radiation.

The dozen observations we have chosen for study are listed in Table 1. Eight were selected based on their peak O^{7+} flux and four on proton flux. There are significant gaps in *ACE* SWEPAM proton density data during several of these observations and, to fill such gaps, we use data from the *Wind* satellite's Solar Wind Experiment (SWE; Ogilvie et al. 1995[4]).

ObsIDs 4215 and 2232 were special cases; both have good SWEPAM proton density data only toward the end of the observation, and *Wind* data, although complete, were collected downstream of Earth in potentially disturbed flow and may, therefore, not be reliable. For ObsID 4215, we used SWICS He density (one-hour sampling) in combination with SWEPAM He/p data[5] (also one-hour sampling, with some interpolation over one- and two-hour gaps) to derive the proton density. ObsID 2232 had a 21 hr gap with neither SWEPAM proton density nor the He/p ratio. That interval is too long for interpolation; thus, we used the *Wind* density. Although $87R_E$ downwind at the time, *Wind* was $44R_E$ to the side of Earth at that time; therefore, its sampling should be relatively undisturbed—an assumption supported by the reasonably good agreement with SWEPAM proton density measurements where the two data sets overlap.

Finally, for ObsID 2255, both satellites are missing eight hours of proton data at the beginning of the observation. *Wind*'s proton densities differ wildly from SWEPAM's where they overlap in time; thus, we estimate missing densities by using SWICS He density and scaling it with a fixed He/p ratio of 0.0414, which is the average of the nearly constant value measured by SWEPAM over the remaining 11 hr of the observation.

Peak ion fluxes—with one-hour binning for protons and two-hour binning for O^{7+}—are listed for each observation in Table 1. For comparison, the typical proton density and solar wind speed at 1 AU in the ecliptic plane are 6.5 cm^{-3} and ∼400 km s^{-1}, yielding a proton flux of 2.6×10^8 s^{-1} cm^{-2}. An O/p abundance ratio of 1/1780 with a 20% O^{7+} fraction, typical of the slow solar wind usually found in the ecliptic plane (Schwadron & Cravens 2000), gives an O^{7+} flux of 2.9×10^4 s^{-1} cm^{-2}. The fluxes in our analysis are, therefore, up to 13 times higher than normal for protons and 32 times higher for O^{7+}.

3. *CHANDRA* DATA

3.1. Data Preparation

X-ray data were retrieved from the *Chandra* archive. All of our observations were recently reprocessed using the *Chandra* Interactive Analysis of Observations (CIAO) software package (Fruscione et al. 2006) under "Repro4"[6] using the latest calibrations (CALDB 4.5.x). Observations made using the Very Faint (VF) mode (see Table 1) received additional filtering to reduce the particle background.[7] After excluding any data from the S4 chip, which has a relatively high and nonuniform particle background and lacks any "stowed" background data (see Section 3.1.2), we identified point sources using the CIAO `wavdetect` tool after creating exposure maps and PSF maps for each observation. To improve the signal-to-noise ratio (S/N), we ran `wavdetect` after filtering on energies of 400–6500 eV, and

[4] Data available at http://web.mit.edu/afs/athena/org/s/space/www/wind/wind.html with 94 s and 1 hr binning.
[5] To avoid confusion between neutral H in the exosphere and ionized H in the solar wind, we use H and p, respectively, as symbols.
[6] http://cxc.harvard.edu/cda/repro4.html
[7] http://cxc.harvard.edu/ciao/why/aciscleanvf.html

set ellsigma=5 (default value is 3) to make the source regions larger than usual.

The resulting source regions near the aim point typically have radii of ∼2″ and capture ≳96% of the point source flux below 1 keV.[8] Regions become progressively larger off-axis and maintain roughly the same encircled energy fraction as the point-spread function broadens, although decreasing S/N makes it harder to detect weak sources. Based on our source detection output, however, any source of more than roughly 30 counts should be detectable anywhere in our fields. Using pessimistic assumptions regarding source variability and spectra, we calculate that the brightest possible undetectable source would contribute less than 1% of the observed SXRB below 1 keV. Combined with extrapolations of observed point source densities near the aim point and their cumulative flux relative to the sub-keV SXRB, we estimate that no more than a couple percent of our cleaned X-ray background comes from point sources at any time. Variability in the light curves of the collective excluded regions is minor; thus, the net effect of residual point source flux on our study of changes in the SXRB should be completely negligible.

3.1.1. Background Reduction

After removing detected point sources, any remaining X-ray emission should be constant, apart from SWCX emission which is mostly below ∼1 keV. The particle background, however, is present at all energies and can rapidly increase during "flares" by factors of 10 or more. These background flares reduce the X-ray S/N, have an unpredictable energy spectrum, and must be removed before spectral fitting. Usually flares are most apparent at energies between 2.5 and 6.5 keV where there is negligible SWCX emission and the quiescent detector background is lowest. We followed the CIAO "Filtering Lightcurves" thread,[9] filtering on energy (350–2000 and 2500–6500 eV), binning by ∼200 s (depending on the number of counts per bin) and running the deflare tool with nsigma usually set to 2.2; ObsID 430 required a value of 1.9 with 400 s binning to get good results. Flare intervals thus identified were removed from the data as were events with chipy=1:8, which corresponds to an area on each ACIS chip that is shadowed by the frame store cover and not exposed to sky emission. Net exposure times after background filtering are listed in Table 1. Note that the back-illuminated S1 and S3 chips have higher low-energy sensitivity and higher detector background than the front-illuminated chips. Figure 2 shows the effects of background filtering on the light curve and spectrum of ObsID 430, which had the highest fractional loss of exposure time.

Several observations not listed in Table 1 were studied up to this point, but then discarded because background flares, although weak, could not be adequately removed. The issue here is not S/N but the fact that the excess detector background has an unknown and potentially variable spectral shape, and therefore intensity changes at a given energy cannot be solely ascribed to varying SWCX emission. The ObsIDs we dropped for this reason are 492, 864, 2787, 3450, 2787, 4162, and 4175.

Although deflare did not flag a problem with ObsID 4215, the 2.5–6.5 keV rate for first 45 ks was ∼15% higher than the remaining 19 ks. This is a small difference, the rates were steady in each phase, and the rates for 1.1–2.0 keV (just above most SWCX emission) and 9–12 keV (pure detector background) had the same ∼11% difference, suggesting that applying separate background normalizations to the two phases (see Section 3.1.2) should largely remove confusion between SWCX and the changing detector background. We therefore chose to keep the data from ObsID 4215, but our analysis results for that observation will have larger uncertainties.

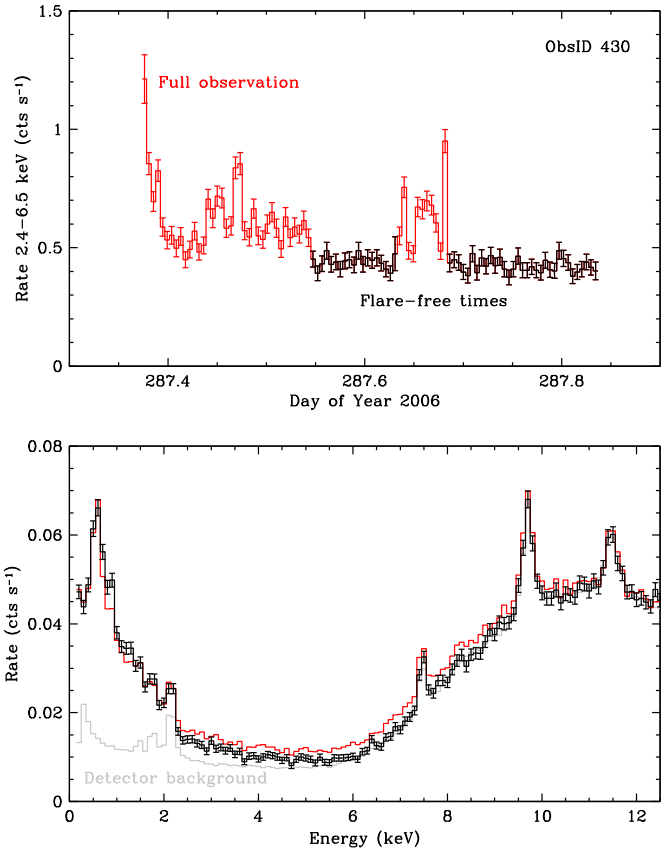

Figure 2. Light curve (400 s bins) and spectrum (100 eV bins) of source-free ObsID 430 data, before and after background-flare removal. The quiescent detector background is also plotted, revealing X-ray emission below ∼6 keV. For clarity, only one spectrum is plotted with error bars. Excess background from the flares (the difference between the red and black curves) is most apparent between roughly 2 and 10 keV. There is also excess background at lower energies, but, in this case, it is hidden by brighter SWCX emission during the flare-free times. (A color version of this figure is available in the online journal.)

After all background-reduction steps were completed, we ran wavdetect again on the cleaned data in order to search for any sources that might have been missed on the first pass. We then visually inspected each field using coarse spatial binning and energy filtering (typically 350–2000 eV) to look for any remaining regions of concentrated emission, including CCD read-out streaks from bright sources. To improve the S/N in four observations of galaxy clusters, we removed the bright cores using large circles. The remaining emission on the clusters' outskirts is constant as it is dominated by hot gas, and point sources are far too weak (distant) to be individually detected or cause significant temporal variations.

Two observations were particularly challenging to prepare. ObsID 3754 viewed the core of the Lagoon nebula, an active star forming region in the Galactic plane. Nearly 200 sources were found, removing roughly half the area of the S3 chip and nearly as much of S2, but many weak and/or diffuse sources undoubtedly remain in our analysis region. The 2.5–6.5 keV

[8] *Chandra* Proposers' Observatory Guide, Chapter 4, http://cxc.harvard.edu/proposer/POG/.
[9] http://cxc.harvard.edu/ciao/threads/filter_ltcrv/

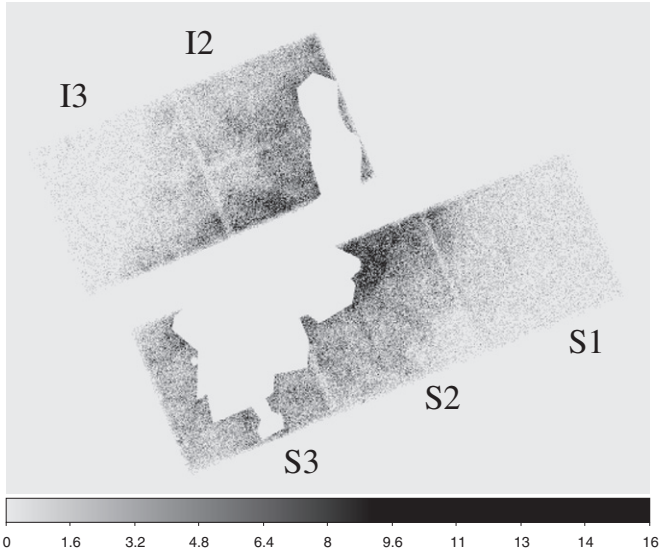

Figure 3. Image of the ObsID 6312 field (W44 supernova remnant) after removing point sources and the brightest areas of diffuse emission. Each ACIS chip is 8.′3 on a side. The S3 and S1 chips are backside-illuminated and have higher QE at lower energies than the front-illuminated chips. The color scale refers to counts per binned pixel (8 × 8) over 300–2000 eV.

light curve is quite clean, however, and we believe that any temporal changes below 2 keV are dominated by SWCX emission rather than source variations.

ObsID 6312 looked at supernova remnant (SNR) W44 and its pulsar wind nebula, a field that contains very bright extended emission. Several point sources were identified and removed but most of the excluded area, a complicated polygon (see Figure 3), was drawn "by eye" while attempting to maximize the S/N of any variable SWCX emission. Remaining diffuse emission from the SNR can be considered constant.

3.1.2. Background Normalization

Although we are primarily interested in X-ray intensity changes, subtracting a properly normalized particle background (i.e., the ACIS "stowed" background) allows us to use a physically realistic model for spectral fitting and more easily account for non-SWCX emission. The particle background varies by roughly a factor of two over the solar cycle but its spectral shape remains essentially constant. Its spatial distribution, however, is nonuniform and energy dependent;[10] thus, it is important to align the background data on the sky to match a given observation (using the `reproject_events` tool) and then remove the same source-exclusion regions.

After X-ray source removal, nearly all ACIS events above ∼9 keV are from high-energy particles, therefore, this portion of the spectrum can be used for background normalization. We use 9.1–12.1 keV, a range where the spectrum is fairly flat at the limits and, therefore, insensitive to small errors in energy calibration, which has a tolerance of ±0.3%.

3.2. Spectral Fitting

After making source- and flare-free event files, we create an Auxiliary Response File (ARF) and Redistribution Matrix File (RMF) for each observation using the `specextract` script. Although each chip's response is different—particularly for the S1 and S3 back-illuminated CCDs—we can use a single ARF and RMF for the entire multi-chip field because the only calibrated fluxes we need to derive are for SWCX emission, which we assume is uniform over the field.[11]

Table 2
SWCX Lines Used in Fitting

Line	Energies (eV)	Fitted Energy (eV)	FWHM (eV)
C VI Lyα	367	367	0
C VI Lyβ,γ,δ	436, 459, 470	460	10
O VII Kα	561, 564, 574	564	0
O VIII Lyα, O VII Kβ	654, 665	660	5
O VIII Lyβ, γ, δ, ϵ	775, 817, 836, 847	810	20
Ne IX Kα	905, 916, 922	913	0
Ne X Lyα	1022	1022	0
Mg XI Kα	1331, 1343, 1352	1340	0

To study the time dependence of SWCX emission, we divide cleaned event files into roughly two-hour bins and extract spectra using `dmextract`. Some bins include gaps of a few hundred seconds from flare filtering; larger gaps ranging from 1500–7800 s (see Figure 4) are used to separate groups of bins. Within each time group, bins are equally divided. Observations with relatively low net effective area (ObsIDs 2232, 3754, and 4215) use longer bins of ∼3 hr (four hours for 2232). ObsID 3012, which starts with extremely high SWCX emission, uses ∼1 hr bins for the first six hours. ObsIDs 544 and 4715, both short observations, are divided into two bins of 1.4 and 0.8 hr, respectively.

To fit the spectra, we use CIAO's modeling and fitting package, Sherpa (Freeman et al. 2001). For each spectrum, we subtract a normalized detector background spectrum and fit the SXRB with the usual model components: an absorbed power law for extragalactic emission with a fixed power-law index of 1.46 and the Galactic column density for that field (Kalberla et al. 2005);[12] absorbed Galactic thermal emission, freezing the Galactic column density and element abundances (solar) and starting with $kT \sim 0.2$ keV; unabsorbed thermal emission from the Local Bubble with solar abundances and starting with $kT \sim 0.1$ keV; and several SWCX lines listed below. An additional hotter thermal component is necessary for a few ObsIDs to account for residual diffuse emission: ObsID 3754 (star formation region), 5801 (galaxy cluster at $z = 0.01230$), 6312 (supernova remnant), and 6433 (star formation region).

Our fitting range is 0.3–6.5 keV, excluding the instrumental Au-M fluorescence line around 2.1 keV. SWCX lines are modeled as Gaussians with the fixed energies and intrinsic widths (no thermal broadening) listed in Table 2. The 460 eV and 810 eV Gaussians represent blends of several high-n Lyman lines over a relatively wide energy range, but each blend is dominated by a single line.

We first establish a baseline fit using combined data from time bins with low SWCX emission; in a few cases, we use the combined spectrum from the complete observation. The fits generally yield reasonable parameter values for the non-SWCX

[10] http://cxc.harvard.edu/cal/Acis/detailed_info.html#background, T. Gaetz, memo, 2014.

[11] As discussed in Section 4.3, most of the variable SWCX emission arises within $\sim 20 R_E$ of *Chandra*. At that distance, a field of view of 8.′3, the width of an ACIS chip, subtends 300 km. Except perhaps near the very nose of the magnetosphere, SWCX emissivity should not vary significantly on that scale.

[12] Using the HEASARC N_H tool (http://heasarc.gsfc.nasa.gov/cgi-bin/Tools/w3nh/w3nh.pl) with the Leiden/Argentine/Bonn map and 0.°5 cone radius.

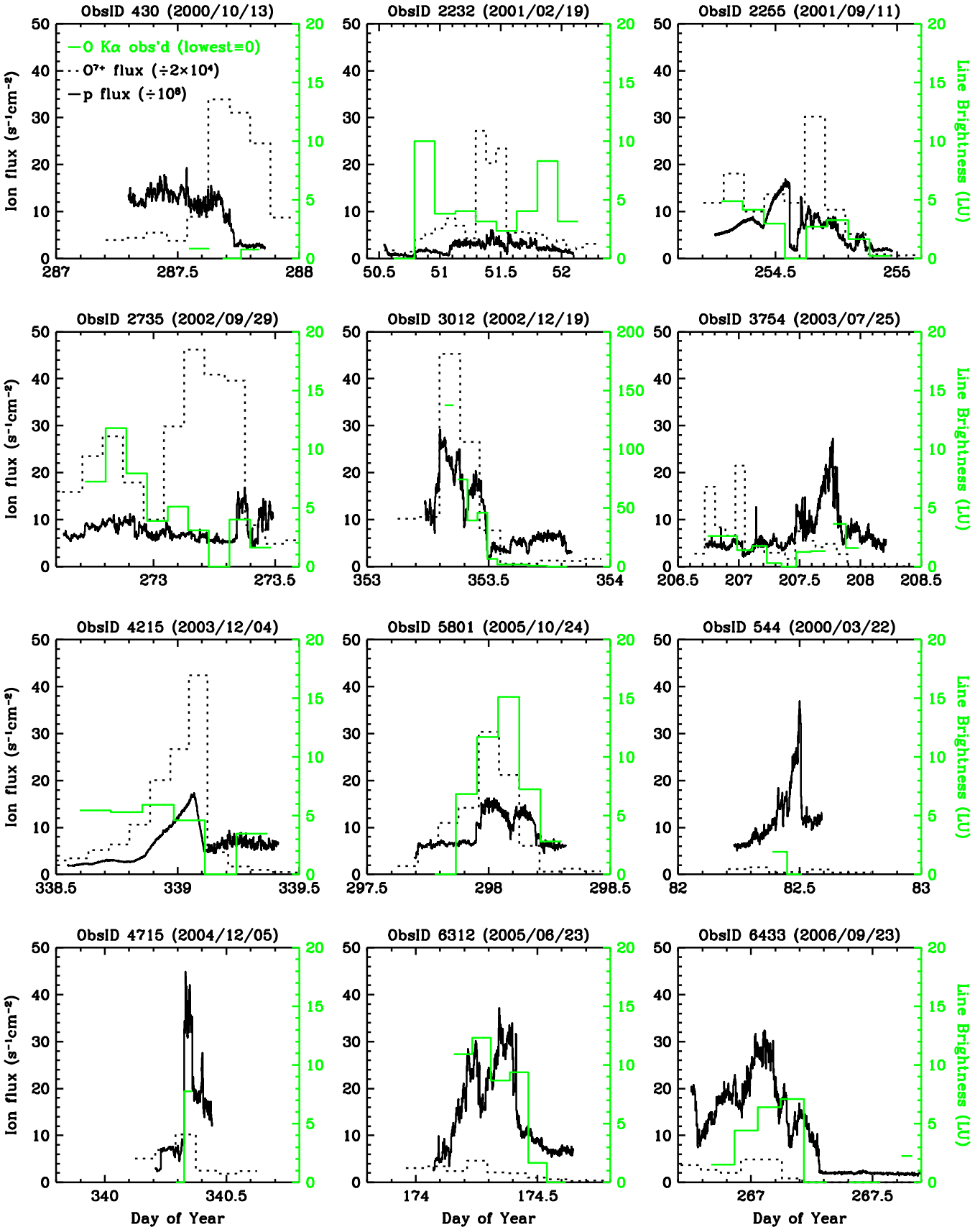

Figure 4. Observed O VII Kα brightness vs. flux of solar wind protons and O^{7+}. Time axis covers two days for ObsIDs 2232 and 3754, one day for all others. Note the different scaling for O VII Kα intensity in ObsID 3012. Breaks in the O Kα traces for ObsIDs 430, 3012, 3754, and 6433 are intervals of prolonged detector background flaring. As can be seen, a high solar wind flux does not necessarily create a high level of observed SWCX emission, which also depends on the observation line of sight.

(A color version of this figure is available in the online journal.)

emission but we do not attempt to derive accurate absolute SWCX line intensities, which is a challenge given the similarity of SWCX and thermal spectra with CCD energy resolution. The important thing is that our cosmic-SXRB model components together with the SWCX lines provide statistically good fits so that any differences between time bins' spectra are well represented by changes in intensities of the fitted SWCX lines. After obtaining a good baseline fit, we freeze all parameters except for the SWCX line amplitudes and fit the spectrum from each time bin separately.

After all fits are complete, we compute each line's brightness in photon cm^{-2} s^{-1} sr^{-1}, or Line Units (LU), by dividing the fitted intensity by the net solid angle of each field. Sherpa's confidence limit determinations are not reliable here because of detector background subtraction and our use of relative measurements; thus, we estimate uncertainties for each line based on the number of counts within 50 eV of the line center (∼1 fwhm) in the observational and detector background data. Count uncertainties are then converted to LU using the appropriate effective area, etc. for each line. Results for O VII Kα are plotted in Figure 4, along with relevant solar wind ion fluxes.

One can see that the proton and O^{7+} fluxes are not always well correlated, which is the result of temporal variations in the relative O abundance and ionization state of the wind. Likewise, periods of high solar wind flux do not always cause a corresponding increase in the observed SXRB. Particularly notable examples include ObsIDs 430, 3754, 544. Although the total level of geocoronal SWCX emission surrounding the Earth does increase in proportion to the flux of highly charged solar wind ions (and even more, because of the compression of the magnetosphere, as discussed at the end of Section 4.1), the SWCX emission seen in a particular observation depends strongly on the line of sight (LOS), as we discuss in the next section.

4. SWCX MODELING

The general approach for geocoronal SWCX modeling is to estimate the flux of solar wind ions near the Earth, combine with a model of exospheric neutral hydrogen density, and then integrate SWCX emissivity along the observer's LOS. The equation for the brightness B_{il} of a SWCX line l from ion i is

$$B_{il} = \frac{1}{4\pi}\int_0^\infty \epsilon_{il}\,dx \ \text{ photons s}^{-1}\text{cm}^{-2}\ \text{sr}^{-1}, \qquad (2)$$

where x is the distance from the observer, in this case *Chandra*. The position-dependent emissivity is given by

$$\epsilon_{il} = v_c n_H n_i y_{il}\sigma_i \ \text{ photons s}^{-1}\ \text{cm}^{-3}, \qquad (3)$$

where v_c is the collision velocity (effectively the ion velocity), n_H is the density of neutral hydrogen in the exosphere, n_i is the relevant ion density, y_{il} is the net line emission yield per CX-excited ion, and σ_i is the total CX cross section for ion i.

Papers that model geocoronal SWCX emission include Snowden et al. (2009) and Robertson et al. (2012). Two other notable efforts are Carter et al. (2011), which models emission during nearly 100 *XMM-Newton* observations that exhibit significant short-term variability in the X-ray background, and Slavin et al. (2013), which models seven *Chandra* observations of the *Chandra* Deep Field North. Both analyses incorporate time-dependent data on solar wind proton density and velocity, and magnetic field strength and orientation. The first analysis makes the simplifying assumption of cylindrical symmetry about the Sun–Earth axis and uses a set of models to separately compute the location of the bow shock, magnetopause, and the velocity and density of solar wind ions in the near-Earth environment. The second paper uses a fully three-dimensional (3D) magnetohydrodynamic code that includes the polar cusps and Earth's tilted, rotating magnetic field. Another difference is that Carter et al. (2011) mostly use fixed element and ion abundances while Slavin et al. (2013) use measured time-dependent values. Our work here uses the more detailed methods of the latter paper, as we discuss below.

4.1. Magnetospheric Modeling

To model the solar wind's interaction with the Earth's magnetosphere, we use the Block-Adaptive-Tree-Solarwind-Roe-Upwind-Scheme code (BATS-R-US, version 20110131; Tóth et al. 2005, 2012), available via the Community Coordinated Modeling Center (CCMC) Runs on Request interface.[13] The BATS-R-US code solves MHD equations in three dimensions using an adaptive grid composed of rectangular blocks of varying sizes in Geocentric Solar Magnetospheric (GSM) coordinates, in which the X axis points from Earth to the Sun and the XZ plane ($Y = 0$) contains the magnetic dipole axis. All coordinate references hereafter use the GSM system. The required inputs are proton density, velocity, temperature, and solar wind magnetic field strength. Earth's magnetic field is approximated by a dipole. The CCMC interface uses *ACE* SWEPAM 64 s proton data and 16 s *ACE* MAG magnetic field data as the defaults, with *Wind* 90 s proton data as backup in case of significant SWEPAM data gaps; short (few-minute) gaps are interpolated. As noted in Section 2, proton density for ObsIDs 2232, 2255, and 4215 is derived in part or whole from one hour SWICS He density and SWEPAM He/p data. ObsID 2735 did not have MAG data so we use magnetic field data from *Wind*. Time-of-flight adjustments from the measurement location to the leading edge of the BATS-R-US simulation volume ($33R_E$ in front of Earth) are applied and all data are rebinned into one-minute increments before input into BATS-R-US. Model runs start one or two hours before the beginning of the *Chandra* observation in order to let the simulation "settle in."

The simulation volume contains ∼2 million cells and extends from −250 to +33 Earth radii (R_E) in X and from −48 to +48 R_E along Y and Z, with block sizes ranging from 0.25 near Earth to 8 R_E at large distances. We bin the output in 20 minute intervals with spatial blocking of 0.5–3 R_E. To reduce file size, the output only covers X from +25 to −50 R_E; geocoronal emissivity along *Chandra*'s LOS is generally negligible outside this volume. The specific outputs we use are: proton density, velocity, and temperature, and a status field that specifies whether the magnetic field in a particular simulation block is closed (status = 3; inside the magnetosphere), open but connected to the north or south poles (status = 2 or 1) in the polar "cusps", or not connected to Earth (status = 0; in the solar wind).

Geocoronal SWCX occurs primarily on the day side of Earth, especially along the bow shock and near the "nose" of the magnetosphere where the solar wind piles up as it encounters the Earth's magnetic field (see Figure 5). Ion density is also high near the polar cusps as ions follow converging magnetic

[13] http://ccmc.gsfc.nasa.gov/requests/requests.php

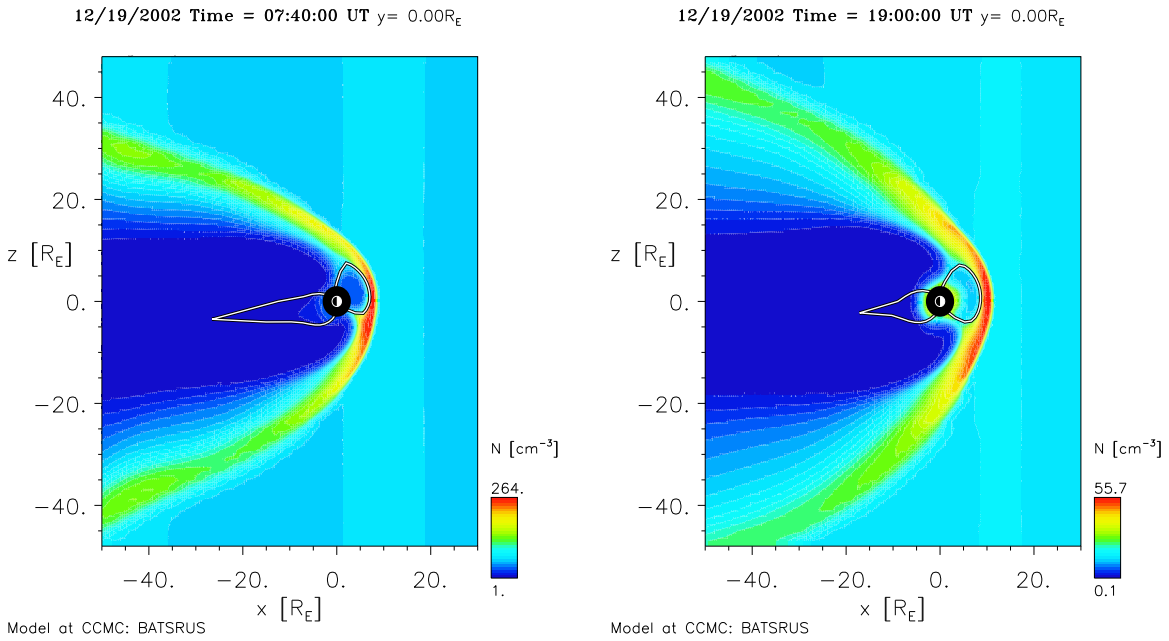

Figure 5. Simulations of proton density in the $Y = 0$ plane during (left) and after (right) a solar wind gust that occurred during ObsID 3012. Note the different color intensity scales and the compression of the magnetosphere and bow shock during the gust. The white trace marks the boundary of closed magnetic field lines. On the day side, this coincides with the magnetopause, while on the night side the magnetopause approximately follows the light/dark blue interface.

(A color version of this figure is available in the online journal.)

field lines. SWCX emissivity is further enhanced near the nose and cusps because ions penetrate relatively deep into the exosphere, where neutral gas density is higher. In contrast, emission is negligible inside the magnetosphere where solar wind is excluded. Emission is more intense during solar wind gusts, not only because of higher ion densities but also because the higher wind flux compresses the magnetosphere, allowing ions to reach denser gas closer to Earth ($n_H \propto r^{-3}$; see below).

4.2. SWCX Emission Calculations

To model SWCX emissivity, we must have values for all of the terms in Equation (3). BATS-R-US does not model minor ions, but we can estimate their densities n_i by scaling the modeled proton density with the implicit assumption that relative ion abundances measured upwind do not change significantly in the near-Earth environment. This should be a sound assumption as the path length for charge exchange with exospheric neutral densities is many thousands of Earth radii and highly charged solar wind ions are little affected by the bow shock. We therefore estimate the density of O^{7+} ions as

$$n_{O^{7+}} = n_p \frac{n_{He}}{n_p} \frac{n_O}{n_{He}} \frac{n_{O^{7+}}}{n_O}, \quad (4)$$

where n_p is taken from the 3D output of the BATS-R-US simulation, the He/p ratio is taken from SWEPAM (or a combination of SWICS He data and binned *Wind* proton data as noted in Table 1), and the other two ratios are taken from SWICS. We use similar equations to estimate the densities of C^{6+}, O^{8+}, and Ne^{9+}, with additional terms for the C/O and Ne/O abundance ratios which are recorded by SWICS. (Ne^{10+} fractions are not recorded in the SWICS archive data; Mg^{11+} and Mg^{12+} fractions are reported, but their uncertainties are extremely large and we do not use them.) All abundance-ratio data receive time-of-flight adjustments from measurement location to Earth center and are assumed to apply throughout the simulation volume. Most SWCX emission occurs within $|X| < 10R_E$, corresponding to only a few minutes of solar wind travel time, which is negligible compared to the one- or two-hour binning of the SWICS data. A few one-bin gaps in SWICS data were filled by interpolation. Ion density is set to zero inside the magnetosphere. Ion bulk velocities and thermal velocities are assumed to be the same as the BATS-R-US proton values.

Charge exchange cross sections and line yields for O VII Kα and Kβ, O VIII Lyα, C VI Lyα, and Ne IX Kα are taken from Wargelin et al. (2004 and references therein). We do not model emission for the blends at 460 and 810 eV because they are weaker, have larger fit uncertainties, and may contain SWCX L-shell emission from Si, S, and Fe ions.

The remaining term in Equation (3) is the density of exospheric neutral H, n_H. Slavin et al. (2013) discuss various density measurements and models and their considerable uncertainties. We use the approximation of Cravens et al. (2001), which is $n_H = 25(10R_E/r)^3\,\mathrm{cm}^{-3}$. Ion data and *Chandra*'s orbital position and pointing direction (at five-minute intervals, from `orbit*eph1.fits` and `angles*eph1.fits` files, respectively) are then read by our `geoCX.f` program that integrates Equation (3) along the LOS out to $50R_E$ from Earth.

4.3. Modeling Results

The resulting model SWCX emission light curves are plotted in Figure 6, along with the integrated O^{7+} and neutral H densities along the LOS. Model line brightness (Equation (3)) is proportional to the integrated *product* of O^{7+} and n_H, but the separate integrals of each term provide a rough measure of how ion and neutral densities change along the LOS during each observation, and from one observation to another. Figure 7 provides additional insight into how O^{7+} and H densities vary along the LOS at a specific time, in this case at the beginning of each observation; *Chandra*'s orbital location and look direction are also plotted.

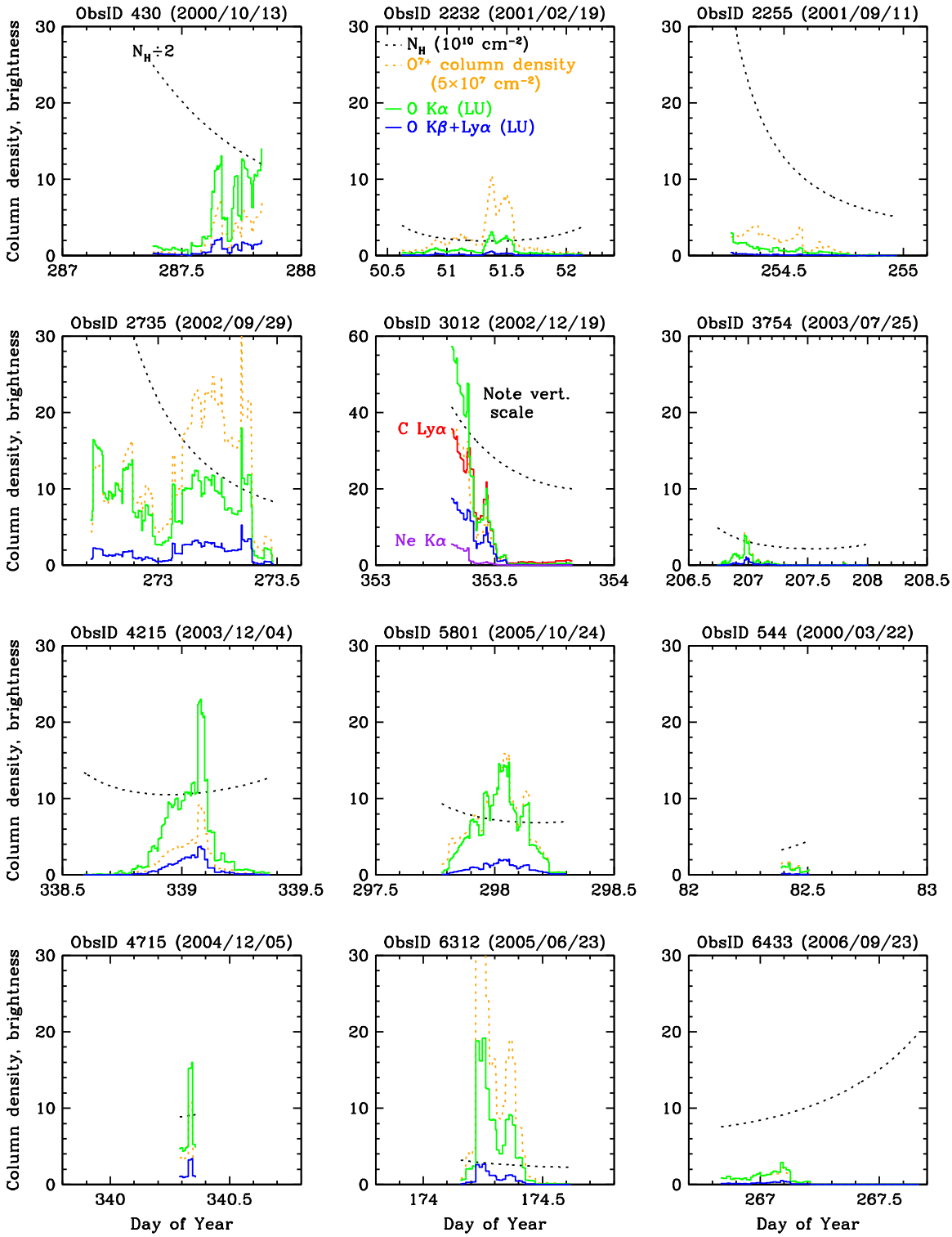

Figure 6. Column densities of exospheric H and solar wind O^{7+} (model inputs) along the LOS, and model brightness predictions for the major oxygen SWCX lines (with O VII Kβ and O VIII Lyα combined). Brightnesses of C VI Lyα and Ne IX Kα were also computed but for clarity are only shown for ObsID 3012. N_H varies smoothly with the changing LOS as *Chandra* orbits the Earth.

(A color version of this figure is available in the online journal.)

In Figure 6, we see that the integrated O^{7+} density along the LOS is well correlated with the net geocoronal O VII Kα emission, as one would expect. The LOS's effect on the exospheric H column density (N_H) and thus geocoronal emission is also apparent, most obviously in the plot for ObsID 2735. For clarity, only model emission for the oxygen lines is plotted, except for ObsID 3012 where we also show curves for C VI Lyα and Ne IX Kα. C Lyα SWCX emission is usually comparable to O VII Kα in brightness, but its observed intensity in CCD spectra is much lower because of decreasing detector efficiency toward low energies. Calibration uncertainties are also much larger and, although we fit C VI Lyα in our spectra, we do not report

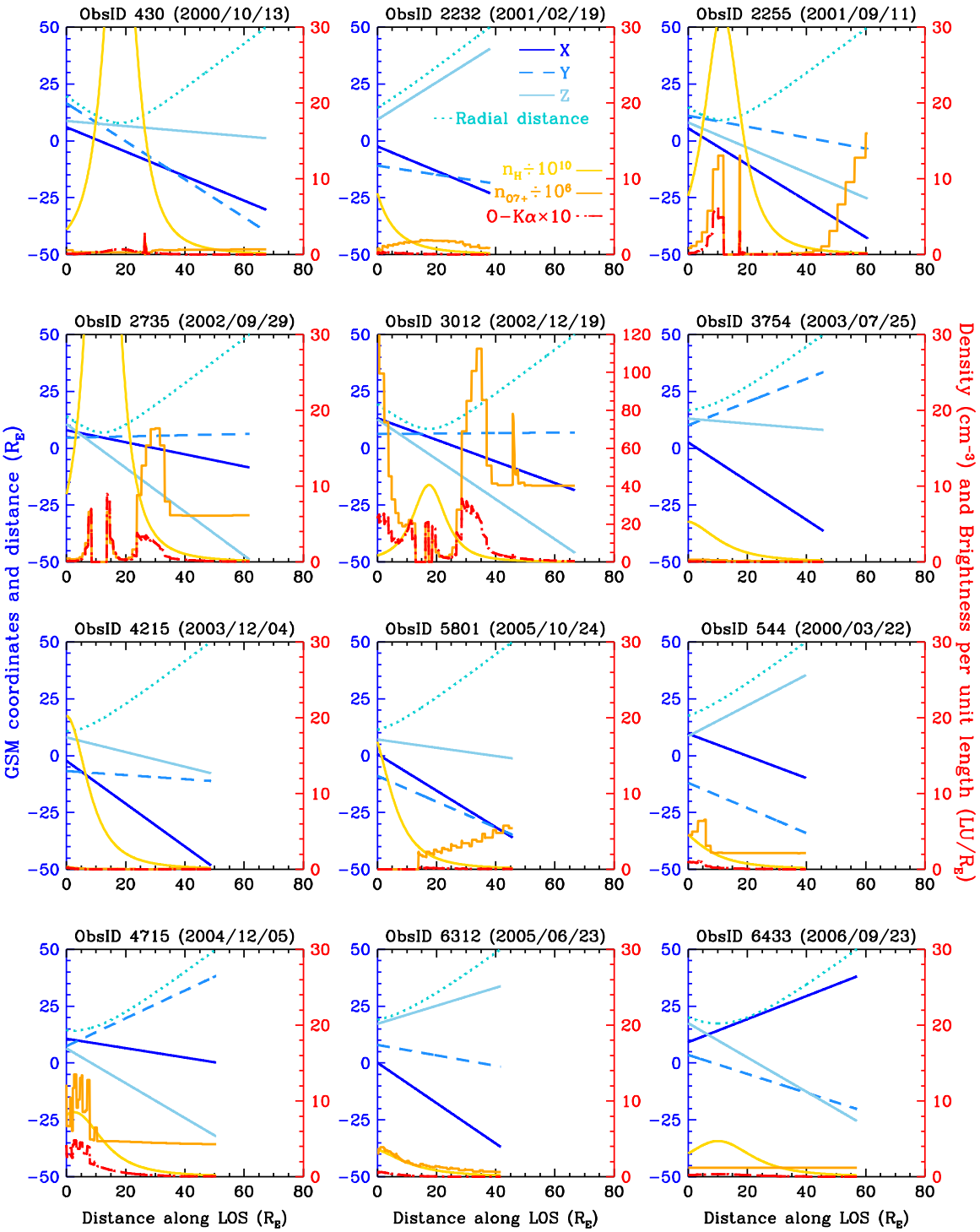

Figure 7. Coordinates and physical conditions along the LOS at the beginning of each observation. Horizontal axis shows distance along the LOS from *Chandra*; emissivities are integrated out to $50R_E$ from Earth. Blueish curves (left axis) mark the 3D position along the LOS and radial distance from Earth. Reddish curves (right axis) show the density of neutral H and O^{7+} along the LOS, along with O VII Kα brightness per unit length in Line Units (LU) per R_E. Gaps where O^{7+} density and O Kα brightness fall to zero are where the LOS passes inside the magnetosphere.

(A color version of this figure is available in the online journal.)

those results. Ne IX Kα is much less bright and only shown for ObsID 3012.

Figures 6 and 7 contain a wealth of information and we discuss only a few examples here. ObsID 3012 has by far the strongest emission because of its large columns of solar wind ions and neutral H along the LOS. At the beginning of the observation (see Figure 7), *Chandra* is orbiting just in front of the magnetosphere ($X = 8.0R_E$; sunward), a little to the side ($Y = 4.6R_E$; trailing side), and above ($Z = 10.7R_E$; north) Earth. Its LOS points slightly outward from the Sun (small negative X slope), but mostly down (south; negative Z slope), passing only $\sim 7R_E$ (dotted blue line) from Earth's center. O^{7+} density is high near *Chandra* and then falls, suddenly becoming zero for a few R_E near $\sim 15R_E$ when the LOS passes inside the

magnetosphere before rising again as the LOS intercepts the flanks of the bow shock at a distance of $\sim 30 R_E$. Line emission varies less drastically along the LOS as the increasing n_H closer to Earth tends to counteract lower ion densities.

At the beginning of ObsID 2255, *Chandra* has a similar orbital position but its LOS is more directly backward and looks mostly through the magnetosphere where n_H is high but $n_{O^{7+}}$ is zero. ObsID 4215 is an even more extreme example: at the beginning of the observation, *Chandra* is inside the magnetosphere and looking nearly straight back (Y and Z slopes near zero) through the magnetosphere so it sees virtually no geocoronal emission. ObsID 6433 is the only observation where *Chandra* is looking at all sunward (positive X slope). In this case, the LOS never passes through the magnetosphere, but nor does it traverse a region of high ion density; thus, line emission is weak. Note that because *Chandra*'s perigee (when it cannot observe because it passes through Earth's radiation belts) is in the south, most of its observing time is spent at positive Z, as for all 12 observations here.

5. MODEL PREDICTIONS VERSUS OBSERVATIONS

In Figure 8, we have rebinned model line brightnesses to match the bins used in our analysis of observational data. Figure 9 directly compares modeled O VII Kα emission with observation for all ObsIDs on the same plot. As in Figure 4, we have set the lowest observed brightness in each observation to zero, except for the two bin ObsID 4715 where we applied a bias to give the best agreement.

As predicted by our model, ObsID 3012 has the strongest SWCX emission. Figure 8 includes data on Ne IX Kα for that observation because of its intensity. Mg XI Kα emission was also strong, with a brightness of 5.4 LU in the first bin (3078 s) and $\sim$0.7 LU over the next three hours. The brightness of the O VII Kβ/O VIII Lyα blend is plotted for every ObsID, but, because its observational error bars are relatively large, we concentrate on the brighter O VII Kα line in Figure 9 and in subsequent discussions. When comparing model predictions for that line with observation there is a roughly equal mix of good, poor, and middling agreement. Below, we list sources of error and uncertainty before examining each observation individually.

Looking first at our model predictions and referring to Equation (3), uncertainties for charge exchange cross sections are typically 30%, with smaller errors for the radiative yields of major SWCX lines. As discussed in more detail in Slavin et al. (2013), uncertainty on exospheric H density beyond $10 R_E$ may exceed a factor of two. This can explain a large portion of the absolute modeling error in any observation, but is less plausible as a cause of the inconsistencies within an observation, such as for ObsID 2735, which begins with good agreement and ends poorly.

The other major source of error in our model is the density of X-ray emitting ions. The SWICS data release notes[14] estimate an uncertainty of 30% for most parameters, although He densities may be underestimated during periods of very high flux, as is often the case here. The one- and two-hour sampling of SWICS data also introduces some unavoidable coarseness to our calculations, and our occasional interpolations of missing data will also add uncertainty. It is very difficult to assign uncertainties to the BATS-R-US predictions for magnetosphere-modified proton density, but whatever they are we expect them to be larger during strong solar wind gusts. Perhaps the largest sources of uncertainty are the exact locations of the magnetopause and bow shock, since small changes can have large consequences when the LOS passes near those boundaries. Modeling the polar cusps is particularly difficult and it has also been suggested (e.g., Ishikawa et al. 2013, based on *Suzaku* data) that solar wind ions can be transported into the inner magnetosphere during magnetic storms, where they can then charge exchange with higher density exospheric gas.

Observational errors arise mostly from counting statistics, fitting errors, and calibration uncertainties. The error bars shown in Figure 8 are based purely on counting statistics, which should be the largest contributor in most cases. Errors may differ substantially from one ObsID to another, not only because of counting rates but also because of differences in effective area $\times$ solid angle, which varies by nearly an order of magnitude (smallest for ObsID 4215 and largest for ObsIDs 3012 and 430).

The last major source of discrepancies between model predictions of geocoronal emission and observed variations in the SXRB is that those variations may also come from heliospheric SWCX. As discussed earlier, heliospheric emission originates over a much larger volume of space than geocoronal SWCX, on scales of several AU rather than tens of R_E, and therefore tends to exhibit variations on longer timescales, but certain viewing geometries can enhance the magnitude of short-term fluctuations. Examples include lines of sight tangent to the "wave fronts" of solar wind density variations, and when a significant fraction of the heliospheric emission arises from a relatively small nearby volume of space, such as the enhanced-density helium focusing cone that Earth passes through each year in early December (see discussion in Slavin et al. 2013).

We now discuss the degree of model-versus-measurement disagreement for each ObsID and possible explanations.

ObsID 430: poor agreement may be because the bow shock is less compressed than in the model, which predicts that *Chandra* is on the flank of the bow shock, roughly in the $X = 0$ plane, with the LOS passing inside and then intercepting the bow shock again on the other side and somewhat behind the Earth. If the bow shock were, in fact, a little farther from the Earth, then the LOS would intercept only lower-density solar wind and the model emission would be lower.

ObsID 2232: in contrast to ObsID 430, the observed X-ray variations are fairly large while the model predictions are small. The model predicts that the LOS passes near but inside the flanks of the bow shock, but perhaps the LOS grazes its edges. Heliospheric emission may also be a factor.

ObsID 2255: observed emission is larger than predicted, but both are fairly low and the differences are not large.

ObsID 2735: agreement is good at first, but observed emission then falls well below predictions for the last half—no obvious explanation.

ObsID 3012: temporal agreement is good, but the observed emission is significantly brighter than predicted. The model predicts that part of the LOS passes just inside the magnetosphere but if it actually stays just outside, where ion densities are very high, this would increase the observed emission.

ObsID 3754: agreement is fairly good.

ObsID 4215: agreement is not very good, though error bars are relatively large. This observation used SWICS

[14] http://www.srl.caltech.edu/ACE/ASC/DATA/level2/ssv3/swics_lv2_v3_release_notes.txt

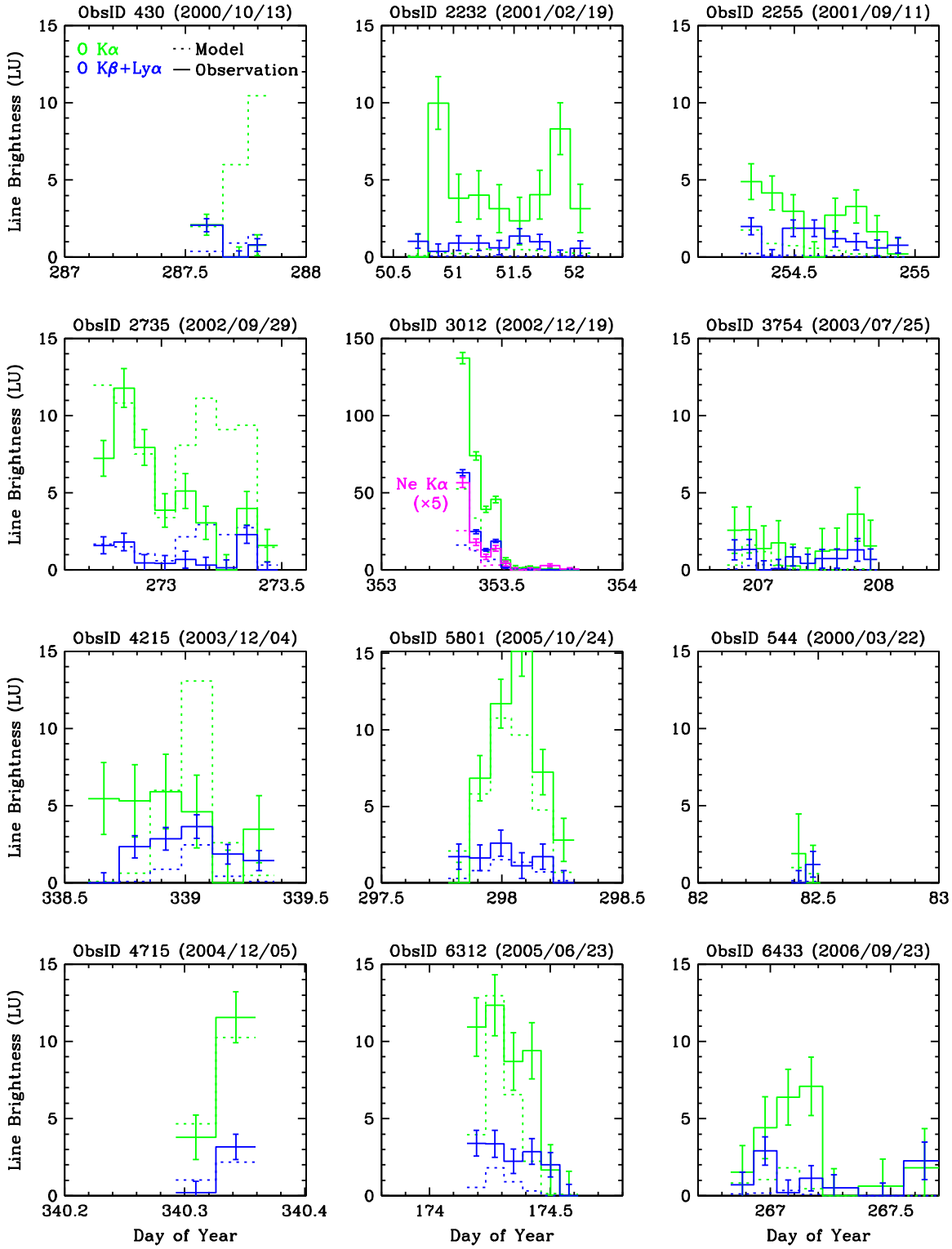

Figure 8. Observed line brightness vs. model predictions, with observational error bars derived from counting statistics as described in Section 3.2. Note the much larger scale for ObsID 3012, where we also plot emission from Ne Kα. As in Figure 4, we set the bias level for observed brightness so that the lowest value is zero, except for ObsID 4715, where it is set to give the best overall agreement. The time axis of ObsID 4715 has also been zoomed for clarity.

(A color version of this figure is available in the online journal.)

He data to infer proton densities (see Section 2) and it suffered from some background-flare contamination (see Section 3.1.1); thus, both model and measurement have additional uncertainties.

ObsID 5801: agreement is good.

ObsID 544: agreement is good.

ObsID 4715: agreement is good.

ObsID 6312: agreement is fairly good.

ObsID 6433: measured brightness is too high, perhaps because of heliospheric emission.

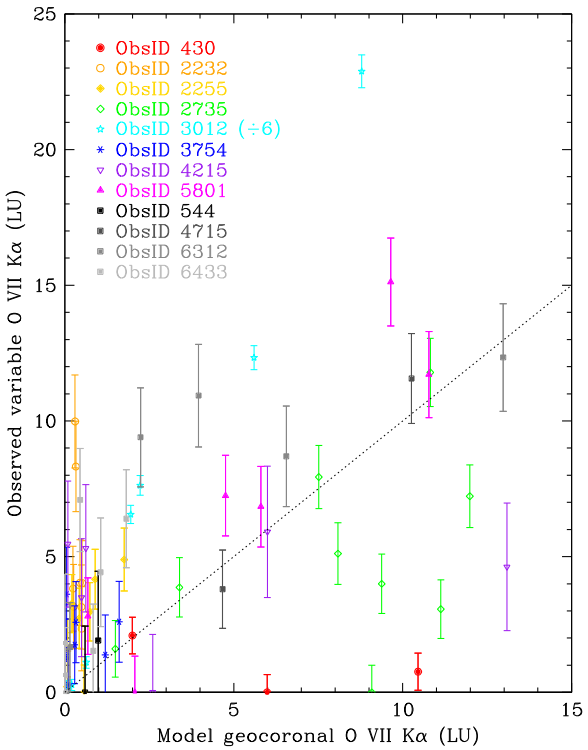

Figure 9. Comparison of observed and predicted geocoronal SWCX emission, plotting the O VII Kα data from Figure 8. Brightnesses for ObsID 3012, both model and observed, were scaled down by a factor of six to fit on the plot. For that ObsID, the observed emission was generally ~2.5× larger than modeled; the dotted line represents a 1:1 observation:model ratio.

(A color version of this figure is available in the online journal.)

Sensitivity to the location of ion density discontinuities is clearly quite high for certain viewing geometries but in cases where solar wind data are reliable and the LOS does not pass tangentially too close to the magnetosphere or bow shock, agreement between model and observation is usually fairly good.

6. CONCLUSIONS AND FUTURE WORK

In this work, we measured variations in the intensity of soft X-ray background emission observed by *Chandra* during intense gusts of solar wind and compared them to predictions of geocoronal SWCX emission using the best available solar wind data and results from state-of-the art BATS-R-US simulations of the solar wind's interaction with the Earth's magnetosphere. Observed intensities of the dominant O VII Kα SWCX emission-line blend were often hundreds of times larger than quiescent geocoronal intensities and greater than the constant cosmic components of the X-ray background. Transient O VII Kα emission in one observation reached a staggering 136 photon s^{-1} cm^{-2} sr^{-1} (LU) averaged over 3000 s, more than an order of magnitude higher than the typical total SXRB in that line. Model predictions agreed fairly well with observations in most cases after taking into account various sources of measurement and modeling error. The largest modeling errors appear to be caused by uncertainties in the exact locations of the magnetopause and bow shock.

In addition to testing the accuracy of magnetospheric simulations, this type of analysis can be used to model geocoronal SWCX emission and subtract it from the SXRB, or identify periods of enhanced emission that will complicate observation analysis and interpretation. Similar methods can be applied to modeling heliospheric emission, though such models have limitations because high quality solar wind data are usually only available near the Earth. Being able to accurately model SWCX emission, or select observations where it is minimal, is important for studies of the local interstellar medium, observations of weak diffuse sources, and attempts to observe oxygen X-ray lines from the warm–hot intergalactic medium (WHIM).

In the near future, the *Astro-H* Soft X-ray Spectrometer microcalorimeter (Mitsuda et al. 2012) will have sufficient energy resolution to cleanly separate lines such as O VII Kβ and O VIII Lyα from each other and improve our ability to distinguish between SWCX and thermal SXRB emission by means of redshifts (0.75 eV for O VII Kα with a 400 km s^{-1} solar wind) and line ratio differences (e.g., SWCX enhancement of the forbidden line component in O VII Kα and of high-n transitions such as O VIII Lyδ). This will, in turn, improve our ability to model SWCX emission, which can then be applied in novel ways, perhaps to measure the density of exospheric H using different lines of sight. This kind of research will, however, not be possible if reliable solar wind data are not available. The *ACE* SWEPAM instrument performance has degraded significantly since its launch in 1997 and no SWICS data have been added to the public archive since a hardware failure in late 2011.

This work was supported by NASA's *Chandra X-ray Center* Archival Research Program under grant SP1-12001X and by the Smithsonian Institution's 2013/2014 Competitive Grants Program for Science. B.W. and M.M. were also supported by NASA contract NAS8-39073 to the *CXC*. We gratefully acknowledge use of SWICS and SWEPAM data provided by the *ACE* Science Center (http://www.srl.caltech.edu/ACE/ASC/), *Wind* data provided by the MIT Space Plasma Group, and magnetosphere simulation results provided by the Community Coordinated Modeling Center at Goddard Space Flight Center. The CCMC is a multi-agency partnership between NASA, AFMC, AFOSR, AFRL, AFWA, NOAA, NSF, and ONR. The SWMF/BATS-R-US model was developed by Tamas Gombosi et al. at the Center for Space Environment Modeling, University of Michigan. We also thank Lutz Rastaetter, Rebekah Evans, and Ofer Cohen for assistance with running and interpreting results from BATS-R-US simulations.

REFERENCES

Bloch, J. J., Jahoda, K., Juda, M., et al. 1986, ApJL, 308, L59
Carter, J. A., Sembay, S., & Read, A. M. 2011, A&A, 527, A115
Cravens, T. E. 1997, GeoRL, 24, 105
Cravens, T. E., Robertson, I. P., & Snowden, S. L. 2001, JGR, 106, 24883
Freeman, P., Doe, S., & Siemiginowska, A. 2001, Proc. SPIE, 4477, 76
Fruscione, A., McDowell, J. C., Allen, G. E., et al. 2006, Proc. SPIE, 6270, 62701V
Fujimoto, R., Mitsuda, K., Mccammon, D., et al. 2007, PASJ, 59, 133
Galeazzi, M., Chiao, M., Collier, M. R., et al. 2014, Natur, 512, 171
Gloeckler, G., Cain, J., Ipavich, F. M., et al. 1998, SSRv, 86, 497
Henley, D. B., & Shelton, R. L. 2008, ApJ, 676, 335
Henley, D. B., & Shelton, R. L. 2010, ApJS, 187, 388
Henley, D. B., & Shelton, R. L. 2012, ApJS, 202, 14
Ishikawa, K., Ezoe, Y., Miyoshi, Y., et al. 2013, PASJ, 65, 63
Kalberla, P. M., Burton, W. B., Hartmann, D., et al. 2005, A&A, 440, 775
Koutroumpa, D., Lallement, R., Raymond, J. C., & Kharchenko, V. 2009, ApJ, 696, 1517
Lallement, R. 2004, A&A, 418, 143
Marshall, F. J., & Clark, G. W. 1984, ApJ, 287, 633
McCammon, D., Burrows, D. N., Sanders, W. T., & Kraushaar, W. L. 1983, ApJ, 269, 107
McComas, D. J., Bame, S. J., Barker, P., et al. 1998, SSRv, 86, 563

Mitsuda, K., Kelley, R. L., Boyce, K. R., et al. 2012, J. Low Temp. Phys., 167, 795
Ogilvie, K. W., Chornay, D. J., Fritzenreiter, R. J., et al. 1995, SSRv, 71, 55
Robertson, I. P., Cravens, T. E., Sibeck, D. G., Collier, M. R., & Kuntz, K. D. 2012, AN, 333, 309
Schwadron, N. A., & Cravens, T. E. 2000, ApJ, 544, 558
Slavin, J. D., Wargelin, B. J., & Koutroumpa, D. 2013, ApJ, 779, 13
Smith, R. K., Bautz, M. W., Edgar, R. J., et al. 2007, PASJ, 59, S141
Smith, R. K., Foster, A. R., Edgar, R. J., & Brickhouse, N. S. 2014, ApJ, 787, 77
Smith, E. J., Marsden, R. G., Balogh, A., et al. 2003, Sci, 302, 1165
Snowden, S. L., Collier, M. R., Cravens, T., et al. 2009, ApJ, 691, 372
Snowden, S. L., Collier, M. R., & Kuntz, K. D. 2004, ApJ, 610, 1182
Snowden, S. L., Freyberg, M. J., Plucinsky, P. P., et al. 1995, ApJ, 454, 643
Tóth, G., Sokolov, I. V., Gombosi, T. I., et al. 2005, JGRA, 110, 12226
Tóth, G., van der Holst, B., Sokolov, I. V., et al. 2012, JCoPh, 231, 870
Wargelin, B. J., Beiersdorfer, P., & Brown, G. V. 2008, CaJPh, 86, 151
Wargelin, B. J., Markevitch, M., Juda, M., et al. 2004, ApJ, 607, 596
Yoshino, T. Y., Mitsuda, K., Yamasaki, N. Y., et al. 2009, PASJ, 61, 805